Atom probe tomography analysis of the reference zircon gj-1: An interlaboratory study

F. Exertier[a,b], A. La Fontaine[a,b,*], C. Corcoran[c], S. Piazolo[c,d], E. Belousova[d], Z. Peng[e], B. Gault[e], D.W. Saxey[f], D. Fougerouse[f,g], S.M. Reddy[f,g], S. Pedrazzini[h], P.A.J. Bagot[i], M.P. Moody[i], B. Langelier[j], D.E. Moser[k], G.A. Botton[j], F. Vogel[l], G.B. Thompson[l], P.T. Blanchard[m], A.N. Chiaramonti[m], D.A. Reinhard[n], K.P. Rice[n], D.K. Schreiber[o], K. Kruska[o], J. Wang[o], and J.M. Cairney[a,b]

[a] School of Aerospace, Mechanical, Mechatronic Engineering, University of Sydney, NSW 2006, Australia
[b] Australian Centre for Microscopy and Microanalysis, University of Sydney, NSW 2006, Australia
[c] Australian Research Council and Centre of Excellence for Core to Crust Fluid Systems/GEMOC, Department of Earth and Planetary Sciences, Macquarie University, NSW 2109, Australia
[d] School of Earth and Environment, University of Leeds, UK
[e] Max-Planck-Institut für Eisenforschung GmbH, Max-Planck-Straße 1, 40237 Düsseldorf, Germany
[f] Geoscience Atom Probe, Advanced Resource Characterisation Facility, John de Laeter Centre, Curtin University, WA 6102, Australia
[g] School of Earth and Planetary Sciences, Curtin University, Perth, WA 6102, Australia
[h] Department of Materials Science and Metallurgy, University of Cambridge, Cambridge CB3 0F3, UK
[i] Department of Materials Science, University of Oxford, Parks Road, Oxford OX1 3PH, UK
[j] Department of Materials Science and Engineering, Canadian Centre for Electron Microscopy, McMaster University, 1280 Main Street West, Hamilton, ON L8S 4M1, Canada
[k] Department of Earth Sciences, University of Western Ontario, 1151 Richmond Street, London, ON N6A 5B7, Canada
[l] Department of Metallurgical & Materials Engineering, University of Alabama,Tuscaloosa, AL 35401, USA
[m] National Institute of Standards and Technology, U.S. Department of Commerce, Boulder, CO 80305, USA
[n] CAMECA Instruments, Inc., 5470 Nobel Dr, Madison, WI 53711, USA
[o] Energy and Environment Directorate, Pacific Northwest National Laboratory, Richland, WA 99352, USA

ABSTRACT

In recent years, atom probe tomography (APT) has been increasingly used to study minerals, and in particular the mineral zircon. Zircon ($ZrSiO_4$) is ideally suited for geochronology by utilising the U-Th-Pb isotope systems, and trace element compositions are also widely used to constrain petrogenetic processes. However, while standard geoanalytical techniques provide information at micrometer scale lengths, the unique combination of chemical/isotopic sensitivity and spatial resolution of APT allows compositional and textural measurements at the nanoscale. This interlaboratory study aims to define the reproducibility of APT data across research facilities and assess the role of different aspects of the atom probe workflow on reproducibility. This is essential to allow correct evaluation of APT results and full utilization of this emerging technique within the geoscience com- munity. In this study, nine samples from the same homogeneous, GJ-1/87 zircon reference grain were sent to nine APT institutes in Germany, the UK, USA, Canada and Australia. After preparing the sample out of a sectioned slab, each institute conducted three different rounds of APT analyses: using (i) unconstrained analysis parameters, (ii) pre-defined analysis parameters, and (iii) interpreting and quantifying a provided dataset. Data such as the measured elemental composition, acquisition parameters, or mass spectrum peak identifications, were recorded and analyzed. We observe a significant variation in the measured composition across this interlaboratory study as well as the number of trace elements identified. These differences are thought to directly result from the user's choice of atom probe data analysis parameters. The type of instrument does not seem to be a critical factor. Consequently, comparison of absolute trace element concentrations on zircon using APT be- tween laboratories is only valid if the same workflow has been ensured.

* Corresponding author at: School of Aerospace, Mechanical, Mechatronic Engineering, University of Sydney, NSW 2006, Australia. E-mail address: alex.lafontaine@sydney.edu.au (A. La Fontaine).

1. Introduction

The accessory mineral zircon ($ZrSiO_4$) is commonly used in geoscience as a geochronometer utilising the U-Th-Pb isotope systems and also as a trace element monitor of geological systems. This is essentially due to its ability to specifically incorporate particular trace elements such as U and Th, but exclude Pb during crystallization as well as the robustness of its lattice structure, composed of isolated SiO_4 tetrahedra, which leads to refractory properties and resistance to weathering (MacDonald, 2013; Möller et al., 2002). The extremely slow diffusivity of solutes, even at high temperature, contributes to zircon's use as a "recording system" (Cherniak et al., 1997; Cherniak and Watson, 2003; Hoskin and Schaltegger, 2003).

Secondary ionization and laser ablation inductively coupled mass spectrometry (SIMS and LA-ICPMS, respectively) are commonly used to measure the trace element composition in zircons. These established geochronology tecniques have the advantage of an excellent chemical detection limit, but has a spatial resolution limited to ≈10 μm (depth resolution can be lower) (Radionova et al., 2015; Schaltegger et al., 2015). In the last decade, studies using advanced electron microscopy, cathodoluminescence and secondary ion mass spectrometry showed that trace elements can be heterogeneously distributed within zircons at the micrometer and sub-micrometer scale in domains affected by crystal-plastic deformation (Kovaleva et al., 2015; Kusiak et al., 2013a; Moser et al., 2009; Piazolo et al., 2012; Reddy et al., 2009; Reddy et al., 2007; Reddy et al., 2006; Timms et al., 2006). Magmatic oscillatory zonation has also been noted (Melnik and Bindeman, 2018). Trace element mobility is also observed in old zircons with high U content due to radiation damage (Harley and Black, 2004). In order to better understand the processes responsible for such heterogeneities and trace element mobility, the geoscience community requires techniques that combine sub-micrometer spatial resolution with high chemical sensitivity and low detection limits. For example, high-resolution ion microprobe (nano-SIMS) can reach a lateral resolution of ≈50 nm while maintaining a

low chemical detection limit, usually below 1µg/g (Kilburn and Wacey, 2015; Kusiak et al., 2013b; Petrelli et al., 2016). In parallel, atom probe tomography (APT) has recently emerged as a technique providing three-dimensional, subnanometer-scale analysis of minerals with a unique combination of chemical/isotopic sensitivity and near-atomic resolution (Gault et al., 2012; Larson et al., 2013). The high electric field intrinsic to APT results in near-perfect ionization, providing high sensitivity and uniformity across all elemental and isotopic species simultaneously during analysis. Detection limits for APT are around 10 ppma, and generally depend on the element and the overall composition of the specimen. In recent years, APT has been increasingly applied to the study of trace element distribution in zircons (La Fontaine et al., 2017; Peterman et al., 2016; Piazolo et al., 2016; Reddy et al., 2016; Valley et al., 2014).

APT relies on the effect of an intense electric field generated at the tip of a 50–100 nm diameter needle-shaped specimen biased to a high voltage, in the range of 3 kV to 11 kV. As this electrostatic field reaches a critical value in the range of 10^{10} Vm^{-1} to 10^{11} Vm^{-1}, the surface atoms are progressively ionized and desorbed from the surface in a process known as field evaporation. Upon laser-assisted field evaporation, the ions are accelerated away from the specimen and projected onto a position-sensitive detector, with a magnification that routinely reaches 10^{6}×. Field evaporation is a thermally-assisted process, critically dependent on the amplitude of the electric field. Time-control of the field evaporation process is gained by superimposing laser pulses to the DC voltage, allowing for time-of-flight mass spectrometry with sub- nanometer spatial resolution. Elemental composition may be calculated by identifying the elemental species associated with individual peaks and measuring and comparing the peak size. Modern atom probe microscopes utilize two main types of flight paths. In one case, a reflectron lens acts as an electrostatic mirror that modifies the flight path of ions having different kinetic energies to improve the mass resolution, while maintaining the field-of-view, but slightly decreasing the overall detection efficiency. Alternatively, a straight flight path enables a higher detection efficiency with a poorer mass resolving power (Clifton et al., 2008; Panayi, 2007).

After some early attempts (Kuhlman et al., 2001; Miller and Russell, 1992), improvements in APT instrumentation and specimen preparation methods have supported a rising interest by the geoscience com- munity in recent years (e.g. Heck et al., 2014; La Fontaine et al., 2017; Peterman et al., 2016; Piazolo et al., 2016; Reddy et al., 2016). Hence, it is timely for the APT community to evaluate the reproducibility of the technique on well-characterized, geological reference materials. It has been widely reported that the composition measured by APT is de- pendent on the analysis conditions, namely the base temperature, the pulsing mode (high-voltage vs. laser), the laser pulse energy, the amplitude of the DC field, detection rate, the type of instrument and detector used (Blum et al., 2016; Costa et al., 2012; Gault et al., 2016; Hashizume et al., 1986; Mancini et al., 2014; Miller and Smith, 1981; Müller et al., 2011; Santhanagopalan et al., 2015; Saxey et al., 2018; Saxey, 2011; Tang et al., 2010; Yao et al., 2011).

In order to monitor experimental biases and long-term reproducibility, the geoscience community relies on well-characterized and homogenous reference zircons that have enabled routine compositional analysis using LA-ICPMS and other microanalytical methods (Belousova et al., 2010). One such reference zircon (GJ-1) was developed by the ARC National Key Centre for Geochemical Evolution and Metallogeny of Continents (GEMOC) and the ARC Centre of Excellence for Core to Crust Fluid Systems (CoE/CCFS) at Macquarie University in Australia. In recent years, it has been widely distributed and used as a chemical reference material for zircon U-Pb geochronology and Hf-isotope analysis (Piazolo et al., 2017).

Here, we report on a interlaboratory APT experiment making use of one grain of this reference zircon GJ-1. To date, few round-robin experiments in APT have been reported in the open literature (Melmed et al., 1979; Nakamura, 1986), but the community is increasingly using this approach to assess analysis methods and techniques. For example, testing the reliability of clustering analysis methods on the same simulated and experimental data sets (Marquis et al., 2016), or the in- fluence of the user on the definition of ranges to translate a mass spectrum into an elemental composition (Hudson et al., 2011; Reinhard et al., 2017). Our effort, coordinated at the University of Sydney, is the first of its kind on a geological material and has utilised nine state-of- the-art instruments spread across Germany, the UK, Canada, USA and Australia. Fragments from the same zircon GJ-1 grain (grain # 87) were cut and sent to the different laboratories for further sample preparation and analysis. The interlaboratory experiment consisted of 3 different rounds of analysis: (i) unconstrained acquisition parameters and data processing; (ii) pre-defined acquisition parameters, and (iii) data processing solely, on a constrained dataset. Here we present the results from this interlaboratory experiment, namely, recording the acquisition parameters, the quality of the mass spectra, the identification of peaks in the mass spectra, and the subsequent measurement of the composition for the primary and trace elements. From our analysis, we derive the critical parameters and lay out what could become best practice in the field. Please note that every single dataset has been made available to the entire scientific community for further processing and data mining in a publicly available repository (see https://apdata.ammrf. org.au/).

2. Experimental procedure

2.1. Interlaboratory experiments

This interlaboratory study was set up as a collaboration between nine APT laboratories in five different countries equipped with four different models of commercial Local Electrode Atom Probes (CAMECA LEAP®[1]), all equipped with UV (λ = 355 nm) laser systems as summarized in Table 1. The single grain of reference zircon was obtained from GEMOC/CCFS at Macquarie University in Australia.

Eleven fragments were sectioned from zircon GJ-1/87 to a size of a few mm^2 each. Those samples were distributed to the participants at the Atom Probe Tomography and Microscopy conference in 2016 (APT&M 2016, Gyeongju, South Korea), without providing any information on the sample, except that it was a reference zircon. All participants received a document that defined the protocol of the interlaboratory study. The participants were asked to share the results listed in Table 2.

2.2. The reference zircon GJ-1/87

The reference zircon used in this study is GJ-1/87 (grain 87): a centimeter size gem quality zircon obtained from GEMOC/CCFS at Macquarie University in Australia, which is thought to originate from African pegmatites with a crystallization age of 608.5 ± 0.4 Ma (Jackson et al., 2004; Piazolo et al., 2017). This well-characterized zircon is exceptionally homogeneous from atomic to millimeter scale, as shown in a recent study utilising APT, LA-ICPMS, transmission Kikuchi diffraction (TKD) and electron backscattered diffraction (EBSD) (Piazolo et al., 2017). Prior to cutting the samples from the single- crystal GJ-1/87, its homogeneity was evaluated by using EBSD (2a). For EBSD, the zircon grain was mechanically polished and then finished with a colloidal silica-water solution. The sample was then carbon coated. EBSD was performed on a Zeiss EVO scanning electron micro- scope (SEM) coupled with a HKL Nordlys Nano high sensitivity EBSD detector and a tungsten source operated at 20kV. AzTec software (Oxford Instruments) was used to index the EBSD patterns, and the results confirmed that GJ-1/87 is a single grain with no noticeable crystal plastic deformation. The sample was then sectioned using a diamond saw into eleven pieces with a section of approximately 1 mm^2 and one piece was given to each participant laboratory. The samples were assigned the following naming convention: Number-Letter-Roman numeral, where: - Number (LEAP base model): 4 (LEAP 4000) or 5 (LEAP 5000)- Letter (detector configuration): R (Reflectron) or S (Straight flight path)
- Roman number (sample iteration): I, II or III for different samples

Most participants independently performed electron imaging and EBSD analysis. Fig. 1b shows images from the SEM and EBSD analyses performed at The University of Sydney (sample piece 4R-I). TKD was also performed on most of the atom probe specimens. TKD analysis on a tip and the associated atom maps from the reconstructed APT dataset is displayed in Fig. 1c (sample piece 4S-II).

No major cracks or other structural disturbances were observed at the micrometer and sub-micrometer scale in the sample shown. However, we note that one participant reported unusual cracks at the sub-micrometer scale that complicated the APT specimen preparation and successful analysis. This sample may have been damaged during or after sectioning. The nominal composition of zircon ($ZrSiO_4$) is 66.6 at. % O, 16.6 at.% Zr and 16.6 at.% Si. Trace element concentrations (Table 3) for the GJ-1/87 zircon sample were acquired in-situ using a Photon Machine Analyte Excite Excimer Laser Ablation System (193 nm) attached to an Agilent 7700cx quadrupole inductively cou- pled plasma mass spectrometer (ICPMS). The working conditions for these analyses were as follows: 5.29 J/cm^2 fluence (or intensity), 50 μm spot size, and a frequency of 5 Hz for the laser pulse rate. The ion species used for normalization were CaO for the reference materials (STD610 & BCR2G) and ZrO_2 for the sample analyses.

[1] The identification of commercial products is to specify the experimental conditions and does not imply any NIST endorsement, recommendation, or imply that they are necessarily the best for the purpose.

Table 1

Instruments used in this interlaboratory experiment. LEAP 5000×S – straight flight path

LEAP 5000×R – reflectron
LEAP 4000× HR – reflectron
LEAP 4000× Si – straight flight path

Table 2

Summary of data provided by participants.

3 instruments 2 instruments 3 instruments 2 instruments

Round 1
Unconstrained (Participants collect 1 or more > 20 M ions datasets)

.pos, .epos and .rhit files Reconstruction details Crystal orientation of the

tips
Details of acquisition

parameters
Range file (.rrng,.rng) Composition measured Sample preparation

method

Round 2
Constrained
Pre-defined conditions: (300pJ – 50K – 250kHz - 1%)
(Participants collected 1 ormore >20Mions datasets)

.pos, .epos and .rhit files Reconstruction details Range file (.rrng,.rng)

Composition measured

Round 3
Ranging
(Participants were provided with a 20 M ions dataset)

Range file (.rrng,.rng) Composition measured

3. Results and discussion

3.1. Peak identification

Species identification in APT is based on the time-of-flight (TOF) of the field-evaporated ions, converted into a mass-to-charge-state ratio, reported in daltons (Da). These data are usually represented as histograms, or 'mass spectra', with peaks corresponding to the detected ions of a specific mass and charge state. The shapes of these peaks result from time delays in the field evaporation process (laser pulsing), or from a spread in the energy either from the emitted ions themselves (e.g. energy deficit in HV pulsing) or through molecular dissociation after initial ionization (Gault et al., 2016). Each of these phenenomena results in a tail trailing the primary peak in the mass spectrum (Gault et al., 2012). This tail can overlap with other peaks from the same or other elements located at higher mass-to-charge state ratios. The background in the mass spectrum is caused by a combination of dark current from the detector, ionization of residual gases from the vacuum chamber by the electrostatic field, and potentially field evaporation of atoms from the specimen by thermal activation at the specimen base temperature (generally 20 K to 80 K). A representative mass spectrum is shown in Fig. 2, and its main features are typical of those acquired from zircons. This mass spectrum was compiled from the sum of all the mass spectra recorded in the unconstrained round and represents over 380 million detected ions.

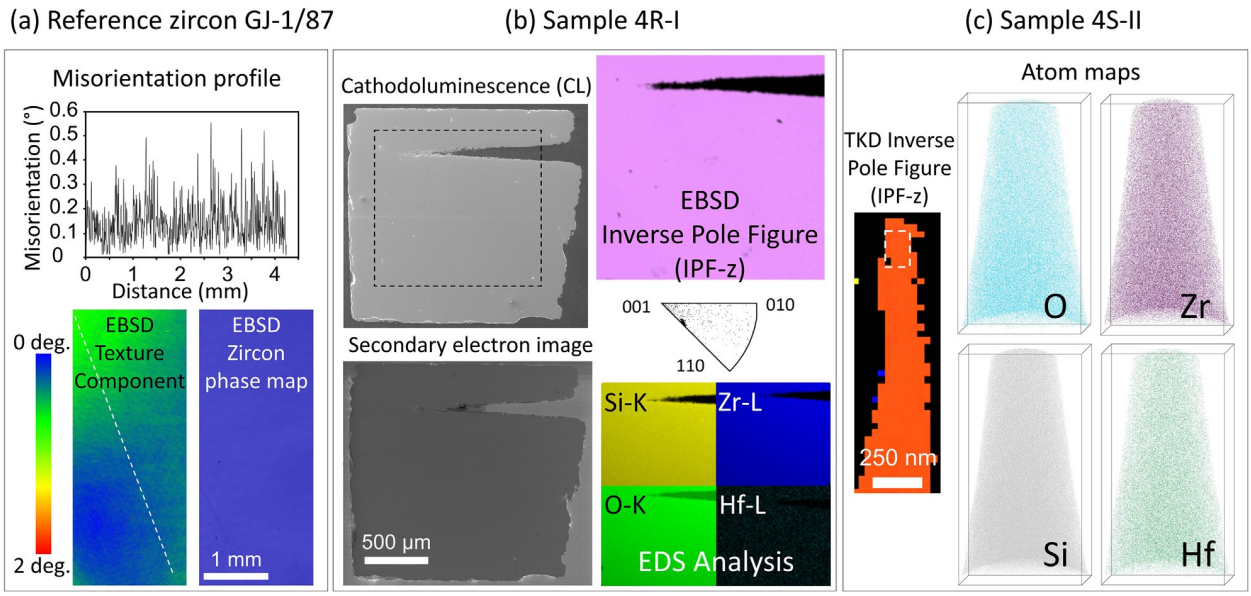

Fig. 1. Multi-scale analysis of reference zircon GJ-1/87, confirming absence of structural disturbances and macro-to-nano homogeneity. (a) EBSD analysis of GJ-1/87 (b) Cathodoluminescence and secondary electron images of sample 4R-I, EBSD and X-ray Energy Dispersive Spectrometry analysis (Arvizu et al., 2011); (c) TKD analysis and atom maps of APT specimen needles from sample 4S-II.

Table 3

Summary of LA-ICPMS trace element concentrations (µg/g) for the GJ-1/87 zircon standard (full data in Table S1).

Analysis	Al	P	Ti	Cu	Ga	Ge	As	Rb	Y	Nb	Hf	Ta	Pb	Th	U
Average	5.38	30.5	4.51	0.10	0.45	0.18	0.21	0.06	197	2.01	5535	0.48	76.9	14.1	222
1σ	0.21	3.0	0.23	0.01	0.02	0.05	0.05	0.01	6.7	0.07	186	0.02	3.3	0.5	8.4

Analysis	La	Ce	Pr	Nd	Sm	Eu	Gd	Tb	Dy	Ho	Er	Tm	Yb	Lu
Average	0.002	15.2	0.03	0.71	1.51	0.89	5.53	1.59	17.3	5.55	23.7	5.46	58.3	8.98
1σ	0.001	0.64	0.002	0.03	0.06	0.03	0.23	0.05	0.6	0.18	0.83	0.18	2.1	0.30

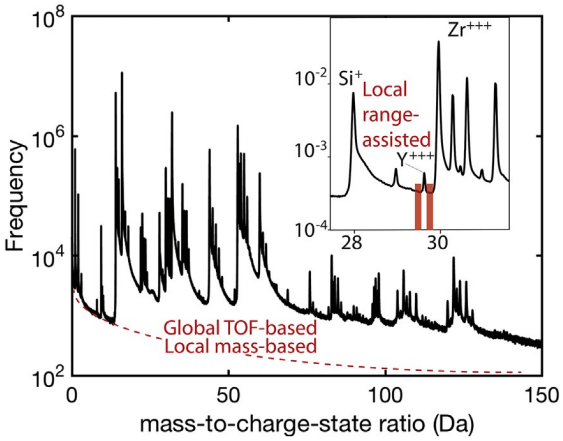

Fig. 2. Mass spectrum histogram from zircon GJ-1/87 obtained from the sum of all mass spectra collected in the unconstrained round. Different background correction models (Global TOF-based, local-mass based and local range-assisted) are highlighted in red. The y axis indicates the ion counts per histogram bin. In the inset this is normalized against the highest peak (O^+). (For interpretation of the references to color in this figure legend, the reader is referred to the web version of this article.)

During the data processing, the user is assisted in a series of auto- mated correction steps by the commercial software package, CAMECA IVASTM, which was used by all participants in the interlaboratory study. For instance, necessary calibration and correction of the measured time- of-flight is performed via application of the methods outlined in Larson et al. (2013) and Sebastian et al. (2001). In an iterative two-step process, the voltage and flight distance (i.e. bowl correction) are successively corrected to optimize the resolution of a single peak in the TOF spectrum. These corrections are followed by a conversion from TOF to mass-to-charge state ratios and further corrections to align known peaks (Larson et al., 2013). Here, we are not discussing the influence of those corrections on the overall composition measurements as they are per- formed blind by all users and are expected to behave in a similar way on all versions of the commercial software used here. We instead focus on the following steps of the data processing, namely the mass spectrum peak identification, ranging and background estimation and correction. The identification of the peaks in the mass spectrum is done manually by the user, who specifies a range of mass-to-charge-state ratios to which a specific type of atomic or molecular ion is associated. This step is colloquially known as peak ranging. These mass ranges are one of the key user inputs to the commercial software package. Peaks ranging and their intensity enable the calculation of the absolute concentrations for each identified element.

The elements identifed by the participants from peak ranging are summarized in Fig. 3. Four elements were identified by all participants for the three rounds: O, Zr, Si and Hf. The majority of participants also identified Y for all rounds. Two groups further identified Th, Er and U and one participant identified more than seven trace elements. The detection limit of APT is influenced by the position and number of peaks associated with a single element in the mass spectrum, which may include peaks arising from multiple isotopes, molecular ion complexes, and different charge states. In addition, the background level varies across the mass spectral range. In ideal situations, the detection limit of APT may be below 10 ppma for some elements (Al for example) and as high as hundreds of ppma for others (U for example). The quantification limit of APT depends indeed on the position of the peak in the mass spectrum and its associated background or noise level. The detection limit is also function of the number of ions collected, and whether the element is homogenously distributed within the material (Gault et al., 2012). The detection of trace elements also depends on the size of the dataset. The peaks for some trace elements, such as Th or Er, can be very challenging to quantify with high confidence because they are often similar in magnitude to the local background noise. Isobaric interference and non-detection of all minor isotopes (i.e. a complete isotopic signature for an element) further complicates confident identification of trace elements. It currently falls to the user to decide whether or not to identify or exclude a given peak with a low signal-to- background ratio. This user choice appeared to be the main factor determining the number of elements identified. There was also no ap- parent trend between the type of instrument used and the number of peaks identified (Fig. 3). This is perhaps surprising as the reflectron- based detector tends to have a superior mass resolving power that could enhance detection of trace elements.

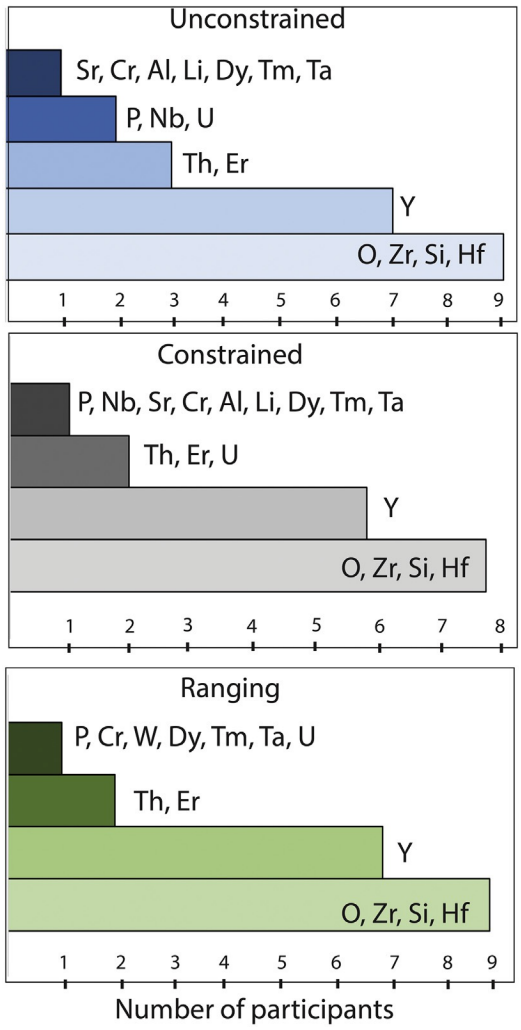

Fig. 3. Elements identified in the study for each stage of analysis. Typical FIB and UHV system impurities (e.g. C, H and Ga) are excluded. The identification of the main elements (O, Zr and Si) and the two main trace elements (Hf and Y; 5535 and 197 μg/g based on LA-ICPMS data) by most of the participants is consistent with previous APT studies of homogeneous zircons in the absence of clustering (La Fontaine et al., 2017; Piazolo et al., 2017; Reddy et al., 2016) (Fig. 3). It is important to note the potential for incorrect ranging in the more detailed trace element analyses, which mostly results from molecular interferences with Zr, Si and O complexes. Essentially, it is up to the participant to push the trace element ranging and confidently address the molecular interferences. In this interlaboratory study, no guidance was given to the participants with respect to data ranging and the difference in participants' geochemistry background is significant, which could explain the distribution observed in the zircon trace element identification.

Fig. 4 shows the concentrations of O, Zr, Si and Hf measured for all three rounds. The full compositions for this study are shown in supplementary Tables S3 and S4. The average O content for all rounds

(≈65 at.%) is below its expected nominal composition and its maximum standard deviation for any single round is ~3 at.%, which corresponds to that of the unconstrained round.

The Zr content is consistently overestimated with an average of ≈18 at.%, while the Si content is closer to its nominal value with an average of ≈16 at.% (see Fig. 4). These results are consistent with previous APT studies of zircons, which reported both a deficit of O and a variation in Zr and Si content (La Fontaine et al., 2017; Peterman et al., 2016; Piazolo et al., 2016; Reddy et al., 2016). Hf composition is quite consistent with LA-ICPMS results at around ≈1000ppma (≈5000 μg/g).

Fig. 4 also shows that the dispersion among the individual measurements decreases between the unconstrained and constrained rounds for O and Si. It shows that the different analysis parameters lead, as expected, to a substantial variation in the resulting composition. The harmonization of the ranging and background correction model de- crease the deviation in the measured composition even further, as shown in Fig. 4. The data points corresponding to the ranging round confirm the importance of user choices during peak ranging, and the

associated background correction models, by showing a greater variation in the measured composition compared to the constrained round using the same range.

3.2. Spectral correction

Once the majority of peaks have been identified and ranged, the background contribution needs to be subtracted in order to obtain an accurate composition. There are three background correction models available in IVAS: (i) global TOF-based which is a background estimate based on the TOF spectrum of the entire dataset that is calculated be- fore reconstruction; (ii) local mass-based correction, which is similar to the global TOF-based estimate but is calculated separately for each mass spectrum created; and (iii) local ranged-assisted background correction, which is calculated for each ranged peak based on the number of counts on either side of the user-defined peak range (Cameca, 2013). The three models are schematically represented in the mass spectrum presented in Fig. 1.

The background correction methods employed by the groups are summarized in supplementary Table S2. Seven out of nine participants used the local ranged-assisted background correction. One participant used a local ranged-assisted background removal method developed in- house, one used the local mass-based correction. The choice of back- ground correction model can be made after the reconstruction. For complex mass spectra such as those from zircon, the background level varies greatly across the TOF range with the contribution of several, overlapping peak tails. Hence, a more localized evaluation of the background for each peak yields more accurate results. Here, most participants chose the local ranged-assisted background correction, hinting towards a possibility to standardize the background correction model.

3.3. Acquisition and reconstruction parameters

Fig. 5 summarizes the principal acquisition parameters used by participants in the unconstrained round. Nearly 20% of the atom probe data sets were collected with a laser energy of 100 pJ and about 70% with a laser energy of 400 pJ and below. The majority of participants used a voltage-controlled average ion detection rate of 1 ion or less per 100 laser pulses, and a specimen base temperature between 45 K and 55K. The laser pulse frequency varied from 125kHz to 250kHz. However, it is irrelevant to compare straight flight path and reflectron- fitted systems in terms of pulse frequency. Often the laser pulse frequency for reflectron-fitted systems is lowered in order to include species with longer times-of-flight (i.e. higher mass-to-charge state ratios).

There is no evident correlation between the acquisition parameters used and the LEAP models (Fig. 5). The laser pulse energy is the parameter that varied the most between participants. It is well known that APT data quality is heavily influenced by the laser pulse energy (Santhanagopalan et al., 2015). The choice of laser pulse energy is often guided by the mass spectrum quality, which is usually measured by its background level, thermal tails behind peaks, and mass resolving power. The data obtained in a typical APT experiment must be re- constructed in order to visualize the 3D volume. Using the simple flight path geometry and the assumption that the specimen is a hemi-spherical cap on a truncated cone, the ion impact detector coordinates can be used to determine the lateral position of the atoms at the surface of the specimen, and the sequence of evaporation is used to deduce the depth of the atoms within the specimen. The most common APT re- construction algorithm is based on the work from Bas et al. (1995), Gault et al. (2011) and Geiser et al. (2009). The reconstruction is generally completed with CAMECA's commercial software package IVAS through semi-automated steps where the user can choose to use

default parameters or calculate their own reconstruction parameters. Optimization of the reconstruction accuracy is widely considered to be a crucial aspect of the APT data processing, as it directly affects the spatial accuracy with which the 3D representation of the field-evaporated volume reflects the true specimen microstructure. In the case we investigate here, where the material is expected to be homogeneous, and we are mainly concerned with composition, the reconstruction step is less critical.
Table S2 shows that the majority of participants calculated their own image compression factor (ICF) and k-factor or used the combi-nation of calculated field evaporation value and atomic volume for Zr. A few participants used the default parameters provided in IVASTM and a single participant used the so-called “tip profile” reconstruction method (Larson et al., 2013).

The reconstruction method principally influences the spatial accuracy of the 3D reconstructed volume and has no impact on the time of flight and the composition measured. The zircon GJ-1/87 sample is perfectly homogenous and as such does not contain any small features that could be used to calibrate the reconstruction, and the nature of zircon field evaporation also does not allow for calibration using crystallographic information. As a result, in this study the spatial accuracy of the 3D volume was not tested.

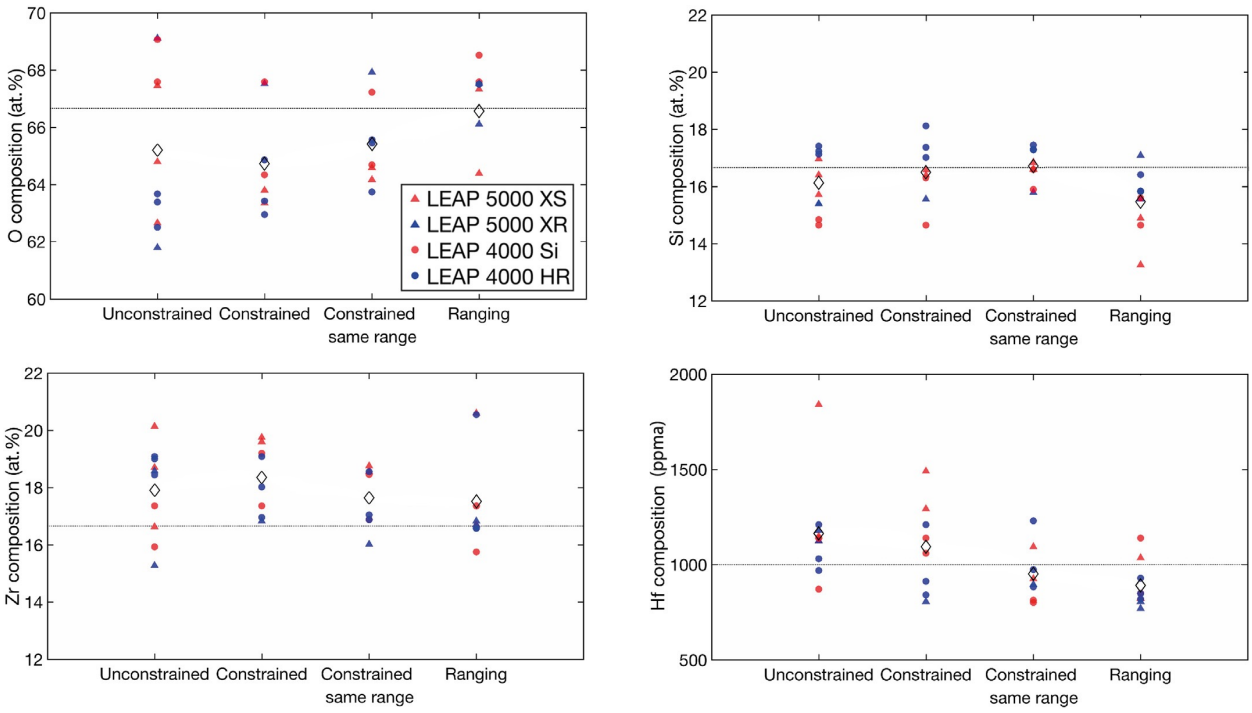

Fig. 4. Concentration measured for the 4 main elements identified by all participants (O, Zr, Si and Hf) in all rounds. The "constrained same range" data points represent the compositions measured in the constrained round using a prescribed same range that was best fitted to the mass spectra. The average composition is displayed as diamonds. The expected stoichiometric values are also displayed in each case (dashed lines).

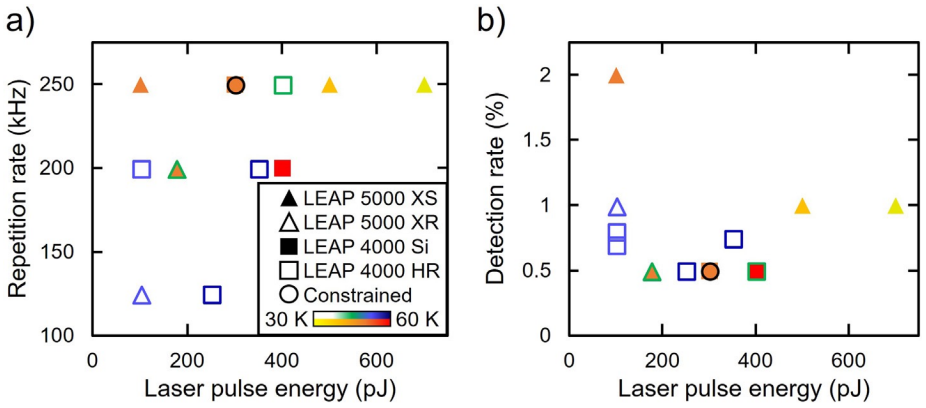

Fig. 5. Acquisition parameters used in the un- constrained round: (a) laser pulse energy vs repetition rate; (b) laser pulse energy vs detection rate. Sample temperature is represented as color bright- ness on a blue/green scale for straight flight-path instrument and on a orange/red scale for reflectron instruments. The black circle represents the acquisition parameters set in the constrained round. (The full data is reported in Supplementary Table S2). (For interpretation of the references to color in this figure legend, the reader is referred to the web version of this article.)

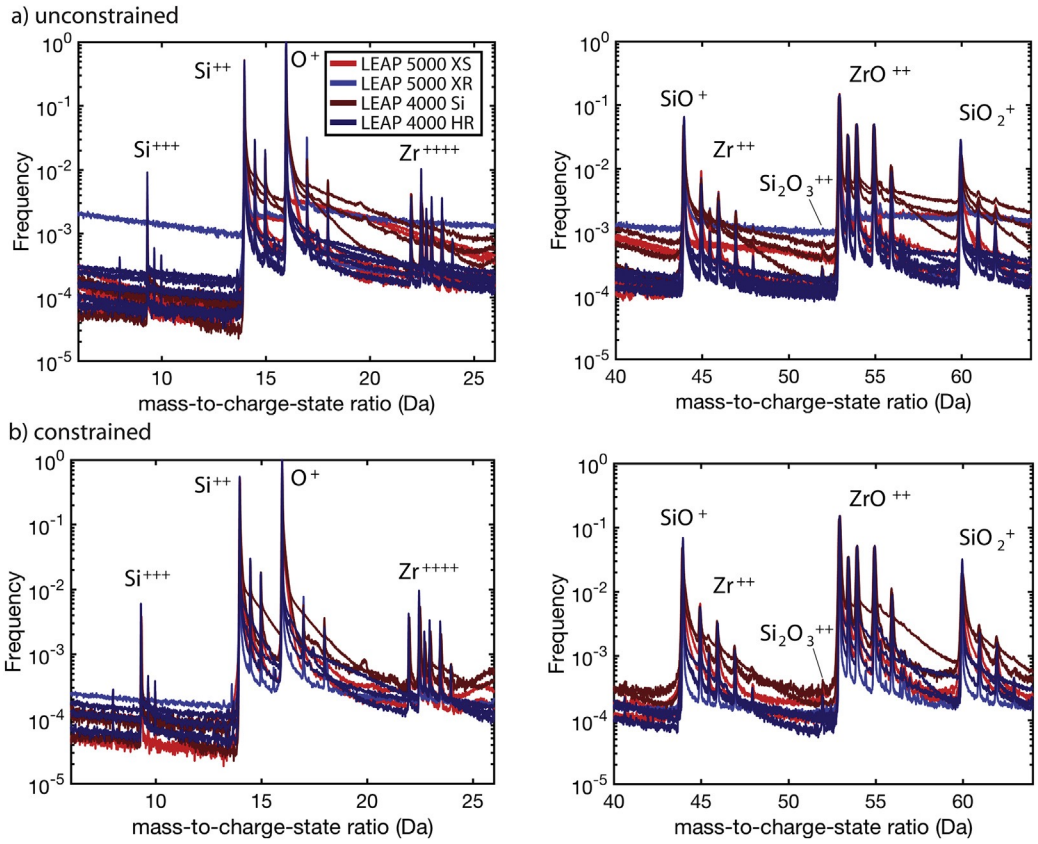

Fig. 6. Normalized mass spectra for (a) unconstrained and (b) constrained analysis rounds.

3.4. Mass spectra and the resulting measured composition

Two close-ups of the mass spectra between 5 Da to 26 Da and 40 Da to 65 Da collected in both the constrained and the unconstrained rounds are shown in Fig. 6(a) and (b) respectively.

There are noticeable differences in the background levels and the extent of thermal tails behind major peaks. These features are influenced by experimental parameters such as the shape of the specimen, the specimen base temperature, the amplitude of the electrostatic field, the laser pulse energy and the instrument vacuum quality. Not all of these factors are easily controllable or reproducible, especially the parameters that are related to the specimen's shape.

A more quantitative way to compare mass spectra from different origins is to look at the signal-to-background ratio for a selected peak versus charge-state-ratio (which gives an indication of the field intensity) or background level around the H peak (informing on the vacuum state of the instrument). Here the signal-to-background ratios were measured for the Y^{3+} peak, which corresponds to one of the major trace elements within the zircon under investigation. The Y^{3+} peak was reported by most of the participants at a level of ≈70 ppma (≈200 μg/ g) on average (similar to the 197μg/g identified by LAICPMS). As shown in the inset in Fig. 7(b), the peak position in the mass spectrum, at 29.66 Da, is clear of major thermal tails or isobaric overlaps. It is plotted against the charge-state-ratio of ZrO (ZrO^{3+}/ (ZrO^{3+} + ZrO^{2+})) in order to reflect the field intensity (Fig. 7(a)). The charge-state-ratio of a peak has previously been shown to qualitatively reflect the intensity of the field (Kingham, 1983; Schreiber et al., 2014), where a higher charge-state-ratio corresponds to higher field. The ZrO species was chosen for its abundance and the absence of isobaric in- terference at the position of its two molecular ions, ZrO^{3+} and ZrO^{2+}.

The signal-to-background ratios are slightly higher for the reflectron-fitted systems, which also display less dispersion than the data from the straight flight path instruments (Fig. 7(a) and (b)). The reflectron-fitted instruments (blue in Fig. 6) benefit in this metric from both a longer flight path and energy filtering of the reflectron lens that both enhances the signal and reduces the native background. The electric field is also more intense in the case of reflectron-fitted systems. This can be explained by a lower detection efficiency as well as a smaller field of view for these systems. In order to sustain an equivalent detection rate, experiments performed with reflectron-fitted systems will require a higher evaporation field compared to a straight flight path system. During an atom probe experiment, the field can be lowered by using a higher laser pulse energy or lower detection rate. The level of background is also slightly higher with a more intense

field, but this seems to have a limited impact on the signal-to-background ratios (Fig. 7(b) and (c)). While the instrument model (4000 vs 5000) does not appear to play a role in the mass spectrum quality, there is some improvement in signal-to-background ratios with reflectron-fitted systems.

A notable 'non-outcome' of this study is the failure at all stages to detect Pb (nominally 11 ppma in bulk sample) let alone measure its isotopic composition. This points to a problem with either instrument detection limits or to micro to nano-scale variations in Pb zoning in the reference material. A similar scenario was also observed in different reference zircon and the monoclinic ZrO_2 mineral, baddeleyite, wherein bulk compositions measured by ICPMS were up to an order of magnitude higher than was measured by APT (Reinhard et al., 2017). Further work on reference materials known to be homogeneous as APT length scales is merited to discriminate among scenarios. At present APT of high Pb (and parent U) zircon (i.e. several hundreds of µg/g) is advisable in geochronological APT studies except in cases where clustering of trace elements is anticipated.

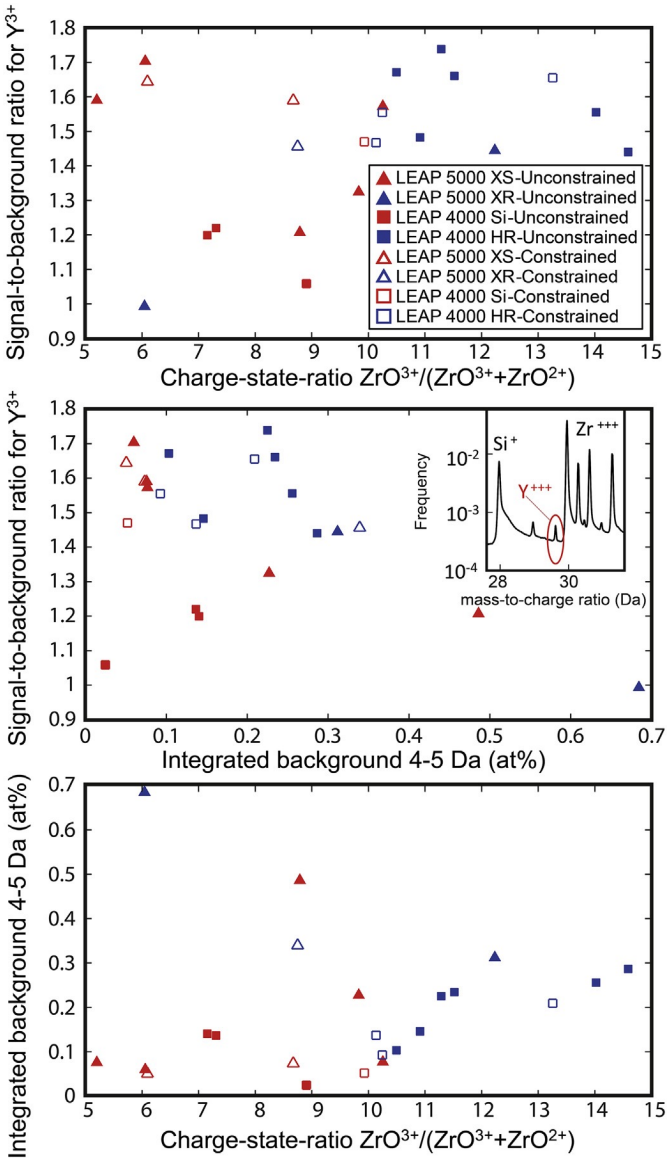

Fig. 7. Measures of background noise and their dependence on the evaporation field, as indicated by the ZrO charge state ratio.

4. Conclusions

The variation in the measured composition across this inter- laboratory study highlights the need to provide guidelines and/or standards for the APT study of specific types of materials. This study confirms the importance of the user's choice in identifying and ranging peaks. The local ranged-assisted background model used by most of the participants is thought to be a good fit for such complicated mass spectra and as a result should be a standard correction for APT of zir- cons. The dispersion of parameters used by our participants to analyze and reconstruct the zircon GJ-1/87 reflects the multiple factors that influence an APT experiment, posing a challenge for the standardization of APT experimental protocols. The type of instrument has a small influence on the data acquired, hence does not seem the most critical factor. Interestingly, in this study, the experiments were performed at higher fields in the reflectron-fitted instruments due to the detection efficiency being lower. Reflectron systems yield slightly better signal-to-background ratios for the selected Y peak examined in this paper. Values of the laser pulse energy or parameters that relate to the specimen geometry are too difficult to control or to be reproduced, and only parameters from the analysis itself should be considered. The background has a strong influence, and better ways to quantify this may be needed. Finally, the charge state ratios seem an interesting para- meter to use for APT data comparison as it can be monitored during the course of the analysis and is only dependent on the physics of the field evaporation.

Acknowledgements

DKS, KK and JW acknowledge support from the U.S. Department of Energy (DOE), Office of Science, Basic Energy Sciences, Materials Science and Engineering Division for financial support of this work. A portion of this research was performed using EMSL, a DOE Office of Science User Facility sponsored by the Office of Biological and Environmental Research at the Pacific Northwest National Laboratory (PNNL). PNNL is a multiprogram national laboratory operated by Battelle for the U.S. DOE.

The Australian Resource Characterisation Facility (ARCF), under the auspices of the National Resource Sciences Precinct (NRSP) – a collaboration between CSIRO, Curtin University and The University of Western Australia – is supported by the Science and Industry Endowment Fund (SIEF RI13-01). ALF and JC acknowledge the facilities and the scientific and technical assistance of the Australian Microscopy & Microanalysis Research Facility at the Australian Centre for Microscopy & Microanalysis at the University of Sydney.

Appendix A. Supplementary data

Supplementary data to this article can be found online at https:// doi.org/10.1016/j.chemgeo.2018.07.031.

References

Arvizu, D., Balaya, P., Cabeza, L., Hollands, T., Jäger-Waldau, A., Kondo, M., Konseibo, C., Meleshko, V., Stein, W., Tamaura, Y., Xu, H., Zilles, R., 2011. Direct solar energy. In: Edenhofer, O., Pichs-Madruga, R., Sokona, Y., Seyboth, K., Matschoss, P., Kadner, S., Zwickel, T., Eickemeier, P., Hansen, G., Schlömer, S., von Stechow, C. (Eds.), IPCC Special Report on Renewable Energy Sources and Climate Change Mitigation, pp. 2011.

Bas, P., Bostel, A., Deconihout, B., Blavette, D., 1995. A general protocol for the re- construction of 3D atom probe data. Appl. Surf. Sci. 87, 298–304.

Belousova, E., et al., 2010. The growth of the continental crust: constraints from zircon Hf-isotope data. Lithos 119 (3), 457–466.

Blum, I., et al., 2016. Dissociation dynamics of molecular ions in high DC electric field. J. Phys. Chem. A 120 (20), 3654–3662.

Cameca, 2013. IVASTM 3.6.6 User Guide.

Cherniak, D.J., Watson, E.B., 2003. Diffusion in zircon. Rev. Mineral. Geochem. 53 (1), 113–143.

Cherniak, D., Hanchar, J., Watson, E., 1997. Rare-earth diffusion in zircon. Chem. Geol. 134 (4), 289–301.

Clifton, P., Gribb, T., Gerstl, S., Ulfig, R.M., Larson, D.J., 2008. Performance advantages of a modern, ultra-high mass resolution atom probe. Microsc. Microanal. 14 (S2), 454–455.

Costa, G.D., et al., 2012. Advance in multi-hit detection and quantization in atom probe tomography. Rev. Sci. Instrum. 83 (12), 123709.

Gault, B., et al., 2011. Advances in the reconstruction of atom probe tomography data. Ultramicroscopy 111 (6), 448–457.

Gault, B., Moody, M.P., Cairney, J.M., Ringer, S.P., 2012. Atom Probe Microscopy. 160 Springer Science & Business Media.

Gault, B., et al., 2016. Behavior of molecules and molecular ions near a field emitter. New J. Phys. 18 (3), 033031.

Geiser, B., et al., 2009. Wide-field-of-view atom probe reconstruction. Microsc. Microanal. 15 (S2), 292–293.

Harley, S.L., Black, L.P., 2004. A revised Archaean chronology for the Napier complex, Enderby Land, from SHRIMP ion-microprobe studies. Antarct. Sci. 9 (1), 74–91.

Hashizume, T., Hasegawa, Y., Kobayashi, A., Sakurai, T., 1986. Atom-probe investigation of III–V semiconductors: comparison of voltage-pulse and laser-pulse modes. Rev. Sci. Instrum. 57 (7), 1378–1380.

Heck, P.R., et al., 2014. Atom-probe analyses of nanodiamonds from Allende. Meteorit. Planet. Sci. 49 (3), 453–467.

Hoskin, P.W.O., Schaltegger, U., 2003. The composition of zircon and igneous and metamorphic petrogenesis. Rev. Mineral. Geochem. 53 (1), 27–62.

Hudson, D., Smith, G., Gault, B., 2011. Optimisation of mass ranging for atom probe microanalysis and application to the corrosion processes in Zr alloys. Ultramicroscopy 111 (6), 480–486.

Jackson, S.E., Pearson, N.J., Griffin, W.L., Belousova, E.A., 2004. The application of laser ablation-inductively coupled plasma-mass spectrometry to in situ U–Pb zircon geo- chronology. Chem. Geol. 211 (1–2), 47–69.

Kilburn, M.R., Wacey, D., 2015. Chapter 1 nanoscale secondary ion mass spectrometry (NanoSIMS) as an analytical tool in the geosciences, principles and practice of analytical techniques in geosciences. R. Soc. Chem. 1–34.

Kingham, D.R., 1983. Charge state of ions in liquid metal field ion sources. Appl. Phys. A Mater. Sci. Process. 31 (3), 161–164.

Kovaleva, E., Klötzli, U., Habler, G., Wheeler, J., 2015. Planar microstructures in zircon from paleo-seismic zones. Am. Mineral. 100 (8–9), 1834–1847.

Kuhlman, K., Martens, R., Kelly, T., Evans, N., Miller, M., 2001. Fabrication of specimens of metamorphic magnetite crystals for field ion microscopy and atom probe micro- analysis. Ultramicroscopy 89 (1), 169–176.

Kusiak, M.A., et al., 2013a. Changes in zircon chemistry during Archean UHT meta- morphism in the Napier complex, Antarctica. Am. J. Sci. 313 (9), 933–967.

Kusiak, M.A., Whitehouse, M.J., Wilde, S.A., Nemchin, A.A., Clark, C., 2013b. Mobilization of radiogenic Pb in zircon revealed by ion imaging: Implications for early Earth geochronology. Geology 41 (3), 291–294.

La Fontaine, A., Piazolo, S., Trimby, P., Yang, L., Cairney, J.M., 2017. Laser-assisted atom probe tomography of deformed minerals: a zircon case study. Microsc. Microanal. 1–10.

Larson, D.J., Prosa, T.J., Ulfig, R.M., Geiser, B.P., Kelly, T.F., 2013. Local Electrode Atom Probe Tomography. Springer Science, New York, US.

MacDonald, J., 2013. Zircon—Earth's timekeeper. Geol. Today 29 (3), 113–117. Mancini, L., et al., 2014. Composition of wide bandgap semiconductor materials and nanostructures measured by atom probe tomography and its dependence on the surface electric field. J. Phys. Chem. C 118 (41), 24136–24151.

Marquis, E.A., et al., 2016. A round robin experiment: analysis of solute clustering from atom probe tomography data. Microsc. Microanal. 22 (S3), 666–667.

Melmed, A.J., Carroll, J.J., Brenner, S.S., 1979. Round-robin atom-probe experiment: preliminary results. Ultramicroscopy 4 (3), 386.

Melnik, O.E., Bindeman, I.N., 2018. Modeling of trace elemental zoning patterns in accessory minerals with emphasis on the origin of micrometer-scale oscillatory zoning in zircon. Am. Mineral. 103 (3), 355–368.

Miller, M., Russell, K., 1992. An APFIM investigation of a weathered region of the Santa Catharina meteorite. Surf. Sci. 266 (1–3), 441–445.

Miller, M., Smith, G., 1981. An atom probe study of the anomalous field evaporation of alloys containing silicon. J. Vac. Sci. Technol. 19 (1), 57–62.

Möller, A., O'brien, P., Kennedy, A., Kröner, A., 2002. Polyphase zircon in ultrahigh-temperature granulites (Rogaland, SW Norway): Constraints for Pb diffusion in zircon. J. Metamorph. Geol. 20 (8), 727–740.

Moser, D., Davis, W., Reddy, S., Flemming, R., Hart, R., 2009. Zircon U–Pb strain chronometry reveals deep impact-triggered flow. Earth Planet. Sci. Lett. 277 (1), 73–79.

Müller, M., Gault, B., Smith, G., Grovenor, C., 2011. Accuracy of pulsed laser atom probe tomography for compound semiconductor analysis. J. Phys. Conf. Ser. 012031 (IOP Publishing).

Nakamura, S., 1986. Round-robin atom probe experiment: preliminary results in Japan Le. J. Phys. Colloq. 47 (C2) (C2-459-C2-464).

Panayi, P., 2007. Atom Probe. (Google Patents).

Peterman, E.M., et al., 2016. Nanogeochronology of discordant zircon measured by atom probe microscopy of Pb-enriched dislocation loops. Sci. Adv. 2 (9), e1601318.

Petrelli, M., Laeger, K., Perugini, D., 2016. High spatial resolution trace element de- termination of geological samples by laser ablation quadrupole plasma mass spectrometry: implications for glass analysis in volcanic products. Geosci. J. 20 (6), 851–863.

Piazolo, S., Austrheim, H., Whitehouse, M., 2012. Brittle-ductile microfabrics in naturally deformed zircon: deformation mechanisms and consequences for U-Pb dating. Am. Mineral. 97 (10), 1544–1563.

Piazolo, S., et al., 2016. Deformation-induced trace element redistribution in zircon re- vealed using atom probe tomography. Nat. Commun. 7.

Piazolo, S., Belousova, E., La Fontaine, A., Corcoran, C., Cairney, J.M., 2017. Trace ele- ment homogeneity from micron-to atomic scale: Implication for the suitability of the zircon GJ-1 as a trace element reference material. Chem. Geol. 456, 10–18.

Radionova, A., Filippov, I., Derrick, P.J., 2015. In pursuit of resolution in time-of-flight mass spectrometry: a historical perspective. Mass Spectrom. Rev. 35 (6), 738–757.

Reddy, S.M., et al., 2006. Crystal-plastic deformation of zircon: a defect in the assumption of chemical robustness. Geology 34 (4), 257–260.

Reddy, S.M., Timms, N.E., Pantleon, W., Trimby, P., 2007. Quantitative characterization of plastic deformation of zircon and geological implications. Contrib. Mineral. Petrol. 153 (6), 625–645.

Reddy, S.M., Timms, N.E., Hamilton, P.J., Smyth, H.R., 2009. Deformation-related mi- crostructures in magmatic zircon and implications for diffusion. Contrib. Mineral. Petrol. 157 (2), 231–244.

Reddy, S.M., et al., 2016. Mechanisms of deformation-induced trace element migration in zircon resolved by atom probe and correlative microscopy. Geochim. Cosmochim. Acta 195, 158–170.

Reinhard, D., Moser, D.E., Martin, I., Rice, K., Chen, Y., Olson, D., Lawrence, D., Prosa, T., Larson, D.J., 2017. Atom probe tomography of phalaborwa baddeleyite and reference zircon BR266-3. Geophys. Monogr. 232 (Microstructural Geochronology).

Santhanagopalan, D., et al., 2015. Effects of laser energy and wavelength on the analysis of LiFePO 4 using laser assisted atom probe tomography. Ultramicroscopy 148, 57–66.

Saxey, D.W., 2011. Correlated ion analysis and the interpretation of atom probe mass spectra. Ultramicroscopy 111 (6), 473–479.

Saxey, D., Reddy, S.M., Fougerouse, D., Rickard, W.D., 2018. The optimization of zircon analyses by laser-assisted atom probe microscopy: insights from the 91500 zircon standard. In: Microstructural Geochronology: Planetary Records Down to Atom Scale, pp. 293–313.

Schaltegger, U., Schmitt, A., Horstwood, M., 2015. U–Th–Pb zircon geochronology by ID- TIMS, SIMS, and laser ablation ICP-MS: Recipes, interpretations, and opportunities. Chem. Geol. 402, 89–110.

Schreiber, D.K., Chiaramonti, A.N., Gordon, L.M., Kruska, K., 2014. Applicability of post- ionization theory to laser-assisted field evaporation of magnetite. Appl. Phys. Lett. 105 (24), 244106.

Sebastian, J.T., Hellman, O.C., Seidman, D.N., 2001. New method for the calibration of three-dimensional atom-probe mass spectra. Rev. Sci. Instrum. 72 (7), 2984–2988.

Tang, F., Gault, B., Ringer, S.P., Cairney, J.M., 2010. Optimization of pulsed laser atom probe (PLAP) for the analysis of nanocomposite Ti–Si–N films. Ultramicroscopy 110 (7), 836–843.

Timms, N.E., Kinny, P.D., Reddy, S.M., 2006. Enhanced diffusion of uranium and thorium linked to crystal plasticity in zircon. Geochem. Trans. 7 (1), 10.

Valley, J.W., et al., 2014. Hadean age for a post-magma-ocean zircon confirmed by atom- probe tomography. Nat. Geosci. 7 (3), 219–223.

Yao, L., Cairney, J., Zhu, C., Ringer, S., 2011. Optimisation of specimen temperature and pulse fraction in atom probe microscopy experiments on a microalloyed steel. Ultramicroscopy 111 (6), 648–651.